

1
2 **Deformation and Strength of Mantle Relevant Garnets: Implications for the**
3 **Subduction of Basaltic-rich Crust**

4 **Cara E. Vennari^{1,2*}, Feng Lin², Martin Kunz³, Masaki Akaogi⁴, Lowell Miyagi², and**
5 **Quentin Williams⁵**

6 ¹Department of Geophysical Sciences, University of Chicago, Chicago, Illinois 60637, USA.

7 ²Geology and Geophysics, University of Utah, Salt Lake City, Utah 84112, USA. ³Advanced
8 Light Source, Lawrence Berkeley National Laboratory, Berkeley, California 94720, USA.

9 ⁴Department of Chemistry, Gakushuin University, Tokyo, Japan. ⁵Earth and Planetary Sciences,
10 University of California Santa Cruz, Santa Cruz, California 95064, USA.

11 **Abstract**

12 Garnet is an important mineral phase in the upper mantle as it is both a key component in
13 bulk mantle rocks, and a primary phase at high-pressure within subducted basalt. Here, we focus
14 on the strength of garnet and the texture that develops within garnet during accommodation of
15 differential deformational strain. We use X-ray diffraction in a radial geometry to analyze texture
16 development in situ in three garnet compositions under pressure at 300 K: a natural garnet
17 (Prp₆₀Alm₃₇) to 30 GPa, and two synthetic majorite-bearing compositions (Prp₅₉Maj₄₁ and
18 Prp₄₂Maj₅₈) to 44 GPa. All three garnets develop a modest (100) texture at elevated pressure
19 under axial compression. Elasto-viscoplastic self-consistent (EVPSC) modeling suggests that
20 two slip systems are active in the three garnet compositions at all pressures studied: {110}<1-
21 11> and {001}<110>. We determine a flow strength of ~5 GPa at pressures between 10 to 15
22 GPa for all three garnets; these values are higher than previously measured yield strengths
23 measured on natural and majoritic garnets. Strengths calculated using the experimental lattice

24 strain differ from the strength generated from those calculated using EVPSC. Prp₆₇Alm₃₃,
25 Prp₅₉Maj₄₁ and Prp₄₂Maj₅₈ are of comparable strength to each other at room temperature, which
26 indicates that majorite substitution does not greatly affect the strength of garnets. Additionally,
27 all three garnets are of similar strength as lower mantle phases such as bridgmanite and
28 ferropericlase, suggesting that garnet may not be notably stronger than the surrounding lower
29 mantle/deep upper mantle phases at the base of the upper mantle.

30 **Keywords:** high-pressure experiment, garnet, texture, strength, radial X-ray diffraction

31 **Introduction**

32 Our understanding of mantle heterogeneity and circulation is derived largely from
33 observations of discontinuities and anisotropy in seismic wave velocities at depth. The upper
34 mantle's seismic heterogeneity has been explained by a combination of preferred orientation of
35 upper mantle minerals, chemically distinct previously subducted material, phase changes in
36 minerals, and partial melting. Small scale heterogeneities have been observed via seismology
37 (e.g., Hedlin et al. 1997), and some of those heterogeneities have been explained as subducted
38 basaltic lithosphere via geochemical and geophysical observations (Davies 1984), and minor
39 seismic reflections (Williams and Revenaugh 2005). By the same token, shape-preferred
40 orientation of (likely basaltic) mantle inclusions have been invoked as one of the possible origins
41 for mantle anisotropy. It has long been appreciated that material of basaltic chemistry is likely a
42 common constituent of the mantle (e.g., Ringwood, 1962); it has been estimated that the upper
43 mantle could contain subducted or delaminated basalt ranging from 5% to 40% (e.g., Allègre &
44 Turcotte, 1986; Cammarano et al., 2009; Hirschmann & Stolper, 1996; Lundstrom et al., 2000;
45 Schmerr et al., 2013; Williams & Revenaugh, 2005; Xu et al., 2008). The significant seismic
46 anisotropy within the Earth's upper mantle is likely due to the shearing and stretching of

47 heterogeneous assemblages within the mantle, including subducted basaltic crust and depleted
48 mantle dunite (McNamara et al. 2001). On the microscopic scale, this deformation of mantle
49 rocks can give rise to crystallographic preferred orientation (texture). Direct observations of
50 subducted slab anisotropy are limited due to the lack of ray paths through subducted slabs, and
51 because the mantle wedge and sub-slab anisotropy obscure slab anisotropy due to upper mantle
52 anisotropy. Nevertheless, there have been a few observations of anisotropy within slabs (e.g.,
53 Tian and Zhao 2012).

54 Hence, garnet-dominated lithologies are relevant to the mantle due to their presence in
55 mafic and high-pressure metamorphic assemblages, such as subducted oceanic crust. Our
56 understanding of the strength of garnets under pressure is derived largely from naturally
57 deformed eclogites where they are resistant to plastic deformation, especially in the presence of
58 weaker minerals like omphacite and quartz that accommodate strain (e.g., Bascou et al. 2001). In
59 low pressure metamorphic facies, garnet is thought to deform via grain boundary sliding rather
60 than intracrystalline deformation (e.g., Zhang & Green 2007). However, in garnet-dominated
61 facies, like at the top of subducted slabs within the transition zone, ~90% of the volume of the
62 crustal material is expected to be majoritic garnet; hence, understanding the deformation of the
63 monomineralic, and especially majorite-bearing, garnet is highly relevant. Garnet has been
64 shown to be strong compared to other mantle materials, indicating that the garnet rich zones (i.e.
65 subducted oceanic crust) may be stronger than the surrounding mantle (Karato et al. 1995).

66 Garnet has a cubic structure with space group $Ia\bar{3}d$. The garnet structure readily
67 incorporates other chemical elements into its crystal structure; this creates extensive solid
68 solutions and changes the stability field of, for example, majoritic garnets (with the introduction
69 of Si). Work on the deformation of pyrope garnets has been conducted using electron

70 backscatter diffraction on naturally deformed eclogite assemblages. Polycrystal plasticity
71 modeling suggests that the $\{110\} \langle 1-11 \rangle$ slip system accommodates over 86% of strain resulting
72 in the $\langle 100 \rangle$ direction aligning with the compression direction (Mainprice et al. 2004). The
73 dominant Burgers vector for naturally deformed silicate garnets in a range of temperature
74 regimes is $\frac{1}{2} \langle 1-11 \rangle$, which most commonly operates on the $\{110\}$ plane (Voegelé et al. 1998a).
75 This supports the results of an experimental deformation study on almandine-rich garnet where
76 the dominant slip systems are $\frac{1}{2} \langle 111 \rangle$ on $\{1-10\}$, $\{11-2\}$ or $\{12-3\}$, or $\langle 100 \rangle$ on $\{010\}$ or
77 $\{011\}$ (Voegelé et al. 1998b). Other deformation experiments on majorite-pyrope garnets with
78 ex situ transmission electron microscopy analysis indicate Burgers vectors of $\langle 100 \rangle$ and
79 $\frac{1}{2} \langle 111 \rangle$ at high pressures and temperatures (Couvry et al. 2011).

80 A study on the strength of garnets has been conducted using high-pressure in situ X-ray
81 diffraction in radial geometry on a natural grossular-rich garnet (Kavner 2007); however, while
82 the strength of this garnet was characterized, the resulting textures and deformation mechanism
83 were not investigated. Similarly, the strength of a majoritic garnet was studied within an axial
84 configuration, but also without investigation of slip system activities (Kavner et al. 2000). Hunt
85 et al. (2010) reported that majorite is slightly weaker than pyrope at lithospheric and upper
86 mantle pressures and temperatures. In a comparison of olivine and pyrope, pyrope was observed
87 to be stronger at upper mantle pressures and temperatures (Li et al. 2006). Recently, Girard et al.
88 (2020) reported high temperature and pressure axial deformation on pyrope for use as a stress
89 sensor material in high pressure and temperature experiments. Hence, we study the high-pressure
90 strength and deformation of natural pyrope and synthetic pyrope-majorite garnets and report their
91 active slip systems up to lower mantle pressures using radial diffraction in the diamond anvil
92 cell. Our room temperature measurements provide constraints on the low-temperature strength

93 and slip systems of garnet, and therefore provide a low temperature bound on the rheologic
94 behavior of garnets, while also providing insights into the compositional dependence of
95 deformation mechanisms and strength.

96 **Methods**

97 Experiments were conducted on three garnets: pyrope (from the UCSC mineral
98 collection, no. 3248, var. rhodolite from Franklin, Macon Co., North Carolina. Samples from this
99 locality have been measured to have a composition of approximately $\text{Prp}_{60}\text{Alm}_{37}$,
100 $\text{Prp}_{58.2}\text{Alm}_{37.1}\text{And}_{1.9}\text{Sps}_{1.5}\text{Grs}_{1.3}$ (Deer et al. 1997) and $\text{Prp}_{60}\text{Alm}_{37.6}\text{Grs}_{2.9}\text{Sps}_{1.8}\text{Uva}_{0.1}$ (Hofmeister
101 et al. 1996). For this study, we will use the “Prp60Alm37” nomenclature, even though there have
102 been other compositional measurements (e.g., Henderson 1931). Based on previous studies that
103 quantified the water content in pyrope-almandine solid solutions from similar metamorphic
104 environments, we estimate an upper bound of the $\text{Prp}_{60}\text{Alm}_{37}$ sample to be 0.04 wt % (Aines and
105 Rossman 1984); this is compatible with the total derived from a wet chemical analysis of a
106 rhodolite from this site (Deer et al. 1997). Two synthetic samples were also used: $\text{Prp}_{59}\text{Maj}_{41}$
107 $(\text{Mg}_3(\text{Al}_{0.59}(\text{MgSi})_{0.41})_2(\text{SiO}_3)_4)$ and $\text{Prp}_{42}\text{Maj}_{58}$ $(\text{Mg}_3(\text{Al}_{0.42}(\text{MgSi})_{0.58})_2(\text{SiO}_3)_4)$. The majorite-
108 bearing samples were synthesized under anhydrous conditions at high pressures, and these
109 aliquots have previously been described and characterized (Akaogi et al. 1987; McMillan et al.
110 1989). Gold (1-5 wt%) was used as the pressure standard (Anderson et al. 1989). $\text{Prp}_{60}\text{Alm}_{37}$ was
111 ground for 1.5 hours with acetone in an agate mortar and pestle, followed by an additional 30
112 minutes with the gold to ensure even dispersal. $\text{Prp}_{59}\text{Maj}_{41}$ and $\text{Prp}_{42}\text{Maj}_{58}$ were loaded with a
113 flake of gold present in the sample chamber. Although grain size was not directly measured prior
114 to compression, crystallite size can provide a proxy for grain size. Crystallite size, which can be
115 determined from Rietveld refinement (e.g., Popa and Balzar 2002) measures the size of

116 coherently diffracting domains within a sample, and was between 150 and 200 Å. A BX90 style
117 diamond anvil cell was used for diffraction with a radial geometry at 300 K. Diamonds with
118 culets of 300 µm were used. The gasket was comprised of kapton with a boron-epoxy insert (50-
119 80 µm thick and ~350 µm in diameter; Merkel & Yagi, 2005); the sample diameter was 60-80
120 µm. Sample material was inserted into the sample chamber with a stainless steel needle. In order
121 to achieve high deviatoric stresses, no pressure medium was included in the sample chamber.
122 Samples were not recovered after compression because the boron epoxy gaskets typically fall
123 apart when the diamond anvil cell is decompressed.

124 Diffraction images were collected at the Advanced Light Source, beamline 12.2.2 (Kunz
125 et al. 2005) using a MAR3450 image plate with X-rays monochromated to 25 keV (wavelength
126 0.4978 Å) and a sample to detector distance of ~330 mm. Wavelength, sample to detector
127 distance, instrument broadening, peak shape, crystallite size, microstructure and texture were
128 calibrated using the NIST standard CeO₂, and initial fits to the instrument calibrations were
129 completed using DIOPTAS (Prescher and Prakapenka 2015), with refinements completed with
130 the MAUD software (Lutterotti et al. 1997).

131 Diffraction images were processed using Fit2D (Hammersley 2016) coupled with
132 fit2D2maud: images were unrolled by integrating over 5° azimuthal arcs, for a total of 72 spectra
133 per diffraction image. Rietveld analysis implemented in the MAUD software (Lutterotti et al.
134 1997) was used to extract texture generally following the procedure for DAC data outlined in
135 Wenk et al. (2014). Textures were calculated using the E-WIMV algorithm within MAUD, with
136 10° resolution for the orientation distribution function, with fiber symmetry imposed. Pole
137 figures and inverse pole figures were smoothed and produced using BEARTEX (Wenk et al.
138 1998).

139 Lattice strain and texture development are modeled together using the elasto-viscoplastic
140 self-consistent method (EVPSC) (Wang et al. 2010). EVPSC is an effective medium method,
141 which treats single grains in an aggregate as inclusions in a homogeneous but anisotropic
142 medium. The properties of the medium are determined by the average of all the inclusions. At
143 each deformation step, the inclusions interact with the medium and the medium is updated when
144 the average strain and stress of all inclusions equal the macroscopic stress and strain. The plastic
145 behavior of the inclusion at the local level is described by a non-linear rate-sensitive constitutive
146 law of various slip systems:

$$\dot{\epsilon}_{ij} = \dot{\gamma}_0 \sum_s m_{ij}^s \left\{ \frac{|m_{kl}^s \sigma_{kl}|}{\tau^s} \right\}^n \text{sgn}(m_{kl}^s \sigma_{kl}) \quad (1)$$

147
148 Where $\dot{\epsilon}_{ij}$ is the strain rate tensor, $\dot{\gamma}_0$ is the reference shear strain rate, τ^s is the critical
149 resolved shear stress (CRSS) value of a slip system s at the reference strain rate, which controls
150 the slip system activation. m_{kl}^s is the symmetric Schmid factor for the slip system s , n is an
151 empirical stress exponent, and σ_{kl} is the local stress tensor. When the stress resolved onto a
152 given slip system is close to the threshold value τ^s , deformation will occur on the slip system.

153 Since pressure and strain increase simultaneously in DAC experiments, it is not possible
154 to separate the pressure and strain hardening effects on CRSS. They are both included in the
155 pressure dependence of the CRSS. In this study, $\tau^s = \tau_0^s + d\tau/dP \cdot P + d^2\tau/dP^2 \cdot P^2$, where
156 τ_0^s is the initial CRSS and $d\tau/dP$ and $d^2\tau/dP^2$ are the first and second order pressure
157 dependences of CRSS. In order to simulate high pressure experimental data, a pressure
158 dependence of the elastic moduli was used. The details for using EVPSC to simulate high
159 pressure data can be found in Lin et al. (2017).

160 **Results and Discussion**

161 **Differential Stress and Elasticity**

162 X-ray diffraction data were collected on Prp₆₀Alm₃₇ up to 31 GPa, and on Prp₅₉Maj₄₁ and
163 Prp₄₂Maj₅₈ up to 44 GPa. Representative experimental and calculated diffraction images are
164 shown in Fig. S1 at 31 or 32 GPa, depending on the sample. Overall, the peaks broaden as
165 pressure is increased; this is due to microstrain (defect structure and strain heterogeneity) within
166 the lattice and likely crystallite size reduction. Using the four diffraction lines (400), (420), (640)
167 and (321), which are strong and do not overlap (1) with other diffraction lines for garnet or (2)
168 with the gold pressure standard, we are able to measure accurate values of lattice strain ($Q(hkl)$);
169 see Text S1 and Fig. S1. The Q -values for these four lines increase at similar rates up to the
170 highest pressures probed (Fig. 1).

171 **Texture and Plasticity**

172 Materials that deform brittlely at room pressure, deform ductilely at elevated pressures; a
173 detailed discussion of this methodology can be found in Wenk et al. (2006). With increasing
174 pressure, modest texturing (plastic deformation) is observed as demonstrated by the development
175 of intensity variations along the Debye rings. As pressure is increased, a (100) maximum
176 develops in the compression direction for all three compositions of garnet. On compression to 30
177 GPa, the pole density increases to a maximum of ~ 1.5 times a random distribution (m.r.d:
178 multiples of random distribution), with a minimum of ~ 0.80 m.r.d. in (111) (Fig. 2) in
179 Prp₆₀Alm₃₇. Prp₅₉Maj₄₁ and Prp₄₂Maj₅₈ also have a maximum of m.r.d. at (100) at 32 GPa
180 (Prp₅₉Maj₄₁ and Prp₄₂Maj₅₈ respectively). The (100) texture remains up to the highest pressures
181 probed for both Prp₅₉Maj₄₁ and Prp₄₂Maj₅₈ (Fig. 2). Interestingly, we do not see a difference in

182 texture with crystal chemistry; Voegelé et al. (1998a) also reported that even across a wide range
183 of chemistry, similar deformation mechanisms were observed in silicate garnets.

184 The (100) normal aligning at high pressures to the compression direction has been
185 observed in other garnets by Mainprice et al. (2004); however, they also found that there was a
186 maximum of (110) poles in the compression direction. These differences indicate that the slip
187 systems described by Mainprice et al. (2004) may not be sufficient to fully model the texture we
188 observe. The pole figure densities (m.r.d.) are low compared to other mantle materials at similar
189 pressures (e.g., MgO and bridgmanite; Merkel, 2002). This has been attributed to the large
190 number (66) of possible slip systems within the garnet structure and/or a change in deformation
191 mechanism to diffusion creep (Mainprice et al. 2004). In our experiments at room temperature,
192 the low m.r.d. values are most likely due to the high number of symmetric variants for slip
193 systems and relatively low strain (~20%). The previous *in situ* study of strength of grossular
194 garnet alluded to possible plastic deformation, but did not characterize textures of deformation
195 mechanisms (Kavner 2007).

196 **EVpsc Modeling and Comparison to Experimental Results**

197 We modeled the evolution of texture and lattice strain as a function of slip system
198 activities using the EVpsc code (Wang et al. 2010). This code is advantageous because it can
199 account for both the elastic and the viscoplastic behavior of the material by modeling lattice
200 strain coupled with grain rotation from dislocation glide rather than only using either elastic (e.g.
201 Elastic Plastic Self-Consistent method, EPSC; (Turner and Tomé 1994) or viscoplastic behaviors
202 (Viscoplastic Self-Consistent method, VPSC; Lebensohn & Tomé, 1994).

203 With EVpsc, we tested seven slip systems : {110}<1-11>, {112}<11-1>, {123}<11-1>,
204 {001}<110>, {011}<100>, {010}<100>, and {110}<1-10>. We imposed a strain rate of $1 * 10^{-4}$

205 s^{-1} as estimated by Marquardt and Miyagi (2015) for a total of ~20% strain for the Prp₆₀Alm₃₇
206 and ~22% strain for Prp₅₉Maj₄₁ and Prp₄₂Maj₅₈; these values were tuned to match the observed
207 texture intensities. We used the shear modulus reported in Sinogeikin and Bass (2000). EVPSC
208 only requires the slip plane normal and slip direction to determine the straining direction of the
209 slip system, not the magnitude of the slip. Hence, we are unable to distinguish between the slip
210 direction (e.g., $\langle 1-11 \rangle$) and the Burgers vector (e.g., $\frac{1}{2}\langle 1-11 \rangle$) Based on the $Q(hkl)$ of (400),
211 (420), (640), and (642) and the texture development with pressure, no single slip system can
212 explain the deformation of pyrope at high pressures (Fig. S2). Only with the activation of two of
213 these slip systems ($\{110\}\langle 1-11 \rangle$ and $\{001\}\langle 110 \rangle$; Fig. 3, Table S1) can we generate the
214 observed textures and lattice strain development in all three garnets. The experimental $Q(hkl)$
215 values and texture are in excellent agreement with the EVPSC modeling (Fig. 3).

216 **Elasticity**

217 In order to compare our results with previous results for other garnets and mantle phases,
218 we use the Voigt approximation for the uniaxial stress component,

$$t = 6G \langle Q(hkl) \rangle \quad (= \sigma_3 - \sigma_1 = \sigma_Y) \quad 2)$$

219 where t is the uniaxial stress component, G is the shear modulus, $Q(hkl)$ is the lattice strain, σ_1
220 and σ_3 are the minimum and maximum stress, and σ_Y is the yield stress (e.g., Singh and
221 Balasingh 1993, 1994; Singh et al. 1998). With this, we are able to estimate the flow strength and
222 measure the elastic limit of the three garnets. We are estimating strength using this technique
223 because it is commonly used in radial diffraction experiments; however, we will discuss that this
224 equation overestimates the true stress in later sections. We utilize a shear modulus of 94.7 GPa
225 and its pressure derivative dG/dP of 1.76 from Chai et al. (1997) for Prp₆₀Alm₃₇ and a shear

226 modulus of 90 GPa and its pressure derivative of 1.3 for both Prp₅₉Maj₄₁ and Prp₄₂Maj₅₈
227 (Sinogeikin and Bass 2002). We find that all three garnets have a flow stress of ~5.5 GPa (Fig. 4,
228 Table S2) using this approximation.

229 In comparing the relative strengths of these garnets, it is apparent that changes to the X
230 and Y cations (where the standard chemistry is X₃Y₂(SiO₃)₄) in these samples have relatively
231 minor effects on the elastic limit of garnet, at least in terms of Mg vs. Fe substitution into the X
232 site and Al vs. Mg and Si substitution into the Y site. The strengths of these garnets are also
233 comparable to those of other mantle phases derived using comparable radial diffraction
234 techniques (Fig. 4). In all the studies we compared, the deformation was imposed using diamond
235 anvil cells and nominally anhydrous starting materials at room temperature. These
236 compositionally-diverse garnets having equivalent strengths at 300 K is in accord with the
237 relative strength measurements of Hunt et al. (2010). Bridgmanite has a comparable flow
238 strength and can accommodate similar differential stress levels up to ~20 GPa (Merkel et al.,
239 2003), while end-member periclase is stronger than garnet at all pressures probed (Merkel,
240 2002). We find that pyrope is stronger than grossular garnet, as reported by Kavner (2007). We
241 have four possible, non-exclusive explanations for this difference in strength: (1) There could be
242 grain size differences between this study and the study of Kavner (2007); (2) there may be an
243 intrinsic strength difference associated with Ca substitution in the X site of the garnet crystal
244 structure; (3) there may be a higher water content/defect concentration in the grossular samples;
245 and/or (4) the azimuthal coverage in these previous experiments may not have allowed for full
246 characterization of the strength of the grossular garnet. With respect to this final explanation, we
247 note that we probe from 0-360° with 5° arcs, while Kavner (2007) utilized 8 discrete angles
248 spanning 180° and fit *Q*-values from those angles.

249 The experimental strength values approximated using equation (2) and those calculated
250 using EVPSC (Fig. 4) are in excellent agreement up to ~10 GPa, and in modest agreement up
251 until the highest pressures probed. The divergence at high pressures is common in high pressure
252 deformation experiments (e.g., Burnley & Zhang, 2008). Although all four of the $Q(hkl)$
253 analyzed in this study were systematically higher than the modeled strength, there is no specific
254 $Q(hkl)$ causing the deviation at higher pressures (Fig. S3).

255 One explanation for this deviation is that an inherent limitation of diffraction-based
256 strength studies is that they are limited by those planes satisfying the diffraction condition. As
257 such, we are unable to measure the lattice strain of all planes within our samples, so we are
258 inherently limiting the input for the approximation using equation (2). By using the strength
259 calculated with EVPSC (Fig. 4), a Reuss-Voigt assumption is not imposed on the data, and we
260 are calculating the true stress. That a difference between calculated and experimental strength
261 exists is demonstrated by our discrepancy between experimental and modeled strengths above
262 ~10 GPa, which increases to ~18% at 44 GPa. Our results support the assertion from Burnley &
263 Zhang (2008) that strengths generated only with experimental lattice strain are not good proxies
264 for the macroscopic stress of the system (Burnley & Zhang 2008). Another explanation for this
265 deviation in t above the flow strength is that equation (2) may not be valid once the material
266 begins to deform plastically. This equation assumes a purely elastic deformation and only utilizes
267 the pressure dependence of G to calculate t , instead of any other constraints which are relevant to
268 the plastic deformation. On the other hand, the strength calculated by EVPSC, utilizes the
269 pressure dependence of G and each slip systems' CRSS; thus yielding a more realistic strength
270 value when both elastic and plastic deformation occurs.

271 **Comparison with Previously Observed Slip Systems in Garnets**

272 The two slip systems, $\{110\}\langle 1-11\rangle$ and $\{001\}\langle 110\rangle$, that are active in $\text{Prp}_{60}\text{Alm}_{37}$,
273 $\text{Prp}_{59}\text{Maj}_{41}$, and $\text{Prp}_{42}\text{Maj}_{58}$ at high pressures have been observed in *ex situ* analysis of deformed
274 garnets with the two most common Burgers vectors being $\langle 110\rangle$ and $\frac{1}{2}\langle 1-11\rangle$. For example,
275 eclogitic garnets deform such that the (100) normal aligns with the compression direction and
276 slip occurs on the $\{110\}\langle 1-11\rangle$ system (Mainprice et al. 2004). Over our experimental pressure
277 range, the majority (~60-64%) of the strain in pyrope is accommodated by this slip system
278 ($\{110\}\langle 1-11\rangle$). This Burgers vector is also consistent with the slip observed by (Voegelé et al.
279 1998b) in $\text{Prp}_{20}\text{Alm}_{73}\text{Sps}_2\text{Grs}_5$ on $\frac{1}{2}\langle 111\rangle$ and by Couvy et al. (2011) in $\text{Prp}_{30}\text{Maj}_{70}$. While
280 Voegelé et al. (1998b) reported equivalent slip in the $\frac{1}{2}\langle 1-11\rangle$ direction on the $\{110\}$, $\{112\}$,
281 and $\{123\}$ planes, Mainprice et al. (2004) reported 86% of the slip in garnets in naturally
282 deformed eclogites occurs via the $\{110\}\langle 1-11\rangle$ slip system. Here, we note that it is difficult to
283 distinguish between the three slip planes $\{110\}$, $\{112\}$, and $\{123\}$ due to the similarity of their
284 textures and development of Q -values. Our selection of the $\{110\}$ plane is partially constrained
285 from the observation of Mainprice et al. (2004). Notably, the $\{110\}\langle 1-11\rangle$ system appears to be
286 active in non-silicate garnets at ambient pressure at least up to temperatures that correspond to
287 ~0.84 of their melting temperature (Karato et al. 1994). Therefore, it appears likely that our 300
288 K deformation experiments access the same primary slip system as is present at high
289 temperatures in other garnets.

290 The other ~40% of the strain is accommodated via the $\{001\}\langle 110\rangle$ system. This slip
291 system has not been observed as a major contributor to the slip in *ex situ* analysis of
292 experimentally or naturally deformed garnets at high pressure/temperature conditions. For
293 example, in natural garnets, of 50 observed dislocations, ~10 dislocations consisted of $\langle 110\rangle$

294 type Burgers vector with glide planes of $\{11-1\}$, $\{22-1\}$ or $\{100\}$ (Voegelé et al. 1998a).
295 Mainprice et al. (2004) used VPSC to identify this slip system $\{001\}\langle 110\rangle$ as accounting for
296 $<1\%$ of the slip in naturally deformed garnets. It has been noted that there can be ambiguity in
297 VPSC calculations; in some cases, more than one slip system can generate the same texture
298 pattern, e.g. CaIrO_3 postperovskite (Miyagi et al. 2008) or MgGeO_3 post perovskite (Merkel et al.
299 2006). In our study, we have an added constraint of the lattice strain, which may account for the
300 difference in relative activities of each slip system. Differences between the secondary slip
301 system of this experiment and observations in garnets probed via TEM could be partially due to
302 the difference in temperature between the high temperatures that the garnets experienced during
303 either the experiments or metamorphism, and our 300 K experiments. Garnets analyzed in
304 Mainprice et al. (2004) experienced pressures over 2.1 GPa and temperatures ranging from 480
305 $^{\circ}\text{C}$ to $>700^{\circ}\text{C}$. If this is the case, $\{110\}\langle 1-11\rangle$ deformation may soften under temperature
306 relative to the $\{001\}\langle 110\rangle$ system. Indeed, it is well known that slip system activities can
307 change with temperature, as for example in ferropericlase (Heidelbach et al. 2003; Immoor et al.
308 2018). Alternatively, the secondary slip system may result from the higher pressures probed in
309 this study compared to the TEM studies: ferropericlase, for example, activates different slip
310 systems below 20-30 GPa and above 60 GPa (Amodeo et al. 2012; Marquardt and Miyagi 2015).

311 **Implications**

312 Shear wave splitting can be generated by the combination of single crystal elastic
313 anisotropy and texturing. Brillouin spectroscopic studies of garnets have demonstrated that they
314 remain close to elastically isotropic to high pressures. The anisotropy factor of pyrope
315 $(2 * C_{44} / (C_{11} - C_{12}) - 1)$ was observed to be -0.02 at ambient conditions, and 0.01 at 14 GPa
316 (Sinogeikin and Bass 2000). With a linear extrapolation to 30 GPa, the anisotropy would be 0.04.

317 P- and S- wave velocities were calculated at 30 GPa with simple shear applied (100% shear
318 strain), and using the extrapolated elastic constants from Sinogeikin and Bass [2000] and the
319 observed texture in Prp₆₀Alm₃₇ (Fig. S4). Overall, the S-wave shear splitting of a polycrystalline
320 aggregate has a maximum of 0.28% in the (100) direction. Since the shear splitting of a rock
321 assemblage depends on each material's contribution to the shear splitting, we expect that pyrope
322 garnet (or, by extension, similarly deforming majoritic garnets) is a silent component in terms of
323 the possible presence of anisotropy in slabs in the upper mantle. Overall, seismic anisotropy
324 observed in subducted slabs is likely not due to cubic solid solutions that are similar to the
325 Prp₆₀Alm₃₇, Prp₅₉Maj₄₁, and Prp₄₂Maj₅₈ garnets that we have characterized. However, andradite
326 (Jiang et al. 2004) and end-member tetragonal majorite (e.g., Pacalo & Weidner, 1997) garnets
327 are less isotropic (as calculated from elastic tensors), and could generate modest contributions to
328 seismic anisotropy in the upper mantle. Nevertheless, a garnet-dominated crust of formerly
329 basaltic chemistry is likely an isotropic cap on top of anisotropic, (Mg,Fe)₂SiO₄-dominated
330 former oceanic lithosphere. Hence, there is likely substantial vertical heterogeneity in the
331 anisotropy of subducted slabs and, based on our study, we anticipate that raypaths that
332 dominantly traverse the crustal component of subducted slabs will show little shear wave
333 splitting; those raypaths with moderately different trajectories sampling the dunite-enriched
334 depleted mantle may sample much more anisotropic media.

335 Our *in situ* analysis of the plastic deformation and flow strength of mantle relevant
336 Prp₆₀Alm₃₇ garnet to 30 GPa and Prp₅₉Maj₄₁, and Prp₄₂Maj₅₈ to 44 GPa at 300 K demonstrates
337 that garnet is relatively strong in comparison to other mantle phases. All three garnet
338 compositions exhibit a flow strength of 5.5 GPa at 8 GPa at 300 K, using both equation (2) and
339 with the EVPSC results. This differs markedly from the previously reported strength of grossular

363 Alliance Center (DE-NA0003858). This research used resources of the Advanced Light Source
364 (beamline 12.2.2) at Lawrence Berkeley National Laboratory which is DOE Office of Science
365 User facility under Contract No. DE-AC02-05CH11231. This research was partially supported
366 by COMPRES, the Consortium for Materials Properties Research in Earth Sciences under NSF
367 Cooperative Agreement EAR 1606856.

368 **References**

- 369 Aines, R.D., and Rossman, G.R. (1984) The hydrous component in garnets: pyrospites.
370 American Mineralogist, 69, 1116–1126.
- 371 Akaogi, M., Navrotsky, A., Yagi, T., and Akimoto, S. (1987) Pyroxene-garnet transformation:
372 Thermochemistry and elasticity of garnet solid solutions, and application to a pyrolite
373 mantle. In M.H. Manghnani and Y. Syono, Eds., High Pressure Research in Mineral Physics
374 pp. 251–260. Washington, D.C.
- 375 Allègre, C.J., and Turcotte, D.L. (1986) Implications of a two-component marble-cake mantle.
376 Nature, 323, 123–127.
- 377 Amodeo, J., Carrez, P., and Cordier, P. (2012) Modelling the effect of pressure on the critical
378 shear stress of MgO single crystals. Philosophical Magazine, 92, 1523–1541.
- 379 Anderson, O.L., Isaak, D.G., and Yamamoto, S. (1989) Anharmonicity and the equation of state
380 for gold. Journal of Applied Physics, 65, 1534–1543.
- 381 Bascou, J., Barruol, G., Vauchez, A., Mainprice, D., and Eglydio-Silva, M. (2001) EBSD-
382 measured lattice-preferred orientations and seismic properties of eclogites. Tectonophysics,
383 342, 61–80.
- 384 Burnley, P.C., and Zhang, D. (2008) Interpreting in situ x-ray diffraction data from high pressure
385 deformation experiments using elastic-plastic self-consistent models: An example using

- 386 quartz. *Journal of Physics Condensed Matter*, 20.
- 387 Cammarano, F., Romanowicz, B., Stixrude, L., Lithgow-Bertelloni, C., and Xu, W. (2009)
- 388 Inferring the thermochemical structure of the upper mantle from seismic data. *Geophysical*
- 389 *Journal International*, 179, 1169–1185.
- 390 Chai, M., Brown, J.M., and Slutsky, L.J. (1997) The elastic constants of a pyrope-grossular-
- 391 almandine garnet to 20 GPa. *Geophysical Research Letters*, 24, 523.
- 392 Couvy, H., Cordier, P., and Chen, J. (2011) Dislocation microstructures in majorite garnet
- 393 experimentally deformed in the multi-anvil apparatus. *American Mineralogist*, 96, 549–552.
- 394 Davies, G.F. (1984) Geophysical and isotopic constraints on mantle convection: An interim
- 395 synthesis. *Journal of Geophysical Research*, 89, 6017–6040.
- 396 Deer, W.A., Howie, A., and Zussman, J. (1997) *Rock-Forming Minerals. Volume 1A:*
- 397 *Orthosilicates*, 2nd ed. The Geological Society, London.
- 398 Girard, J., Silber, R.E., Mohuiddin, A., Chen, H., and Karato, S.I. (2020) Development of a
- 399 stress sensor for in-situ high- pressure deformation experiments using radial x-ray
- 400 diffraction. *Minerals*, 10.
- 401 Hammersley, A.P. (2016) FIT2D: A multi-purpose data reduction, analysis and visualization
- 402 program. *Journal of Applied Crystallography*, 49, 646–652.
- 403 Hedlin, M.A.H., Shearer, P.M., and Earle, P.S. (1997) Seismic evidence for small-scale
- 404 heterogeneity throughout the Earth's mantle. *Nature*, 287, 145–150.
- 405 Heidelberg, F., Stretton, I., Langenhorst, F., and Mackwell, S. (2003) Fabric evolution during
- 406 high shear strain deformation of magnesiowüstite ($\text{Mg}_{0.8}\text{Fe}_{0.2}\text{O}$). *Journal of Geophysical*
- 407 *Research: Solid Earth*, 108.
- 408 Henderson, E.P. (1931) Notes on some minerals from the rhodolite quarry near Franklin, North

- 409 Carolina. *American Mineralogist*, 16, 563–568.
- 410 Hirschmann, M.M., and Stolper, E.M. (1996) A possible role for garnet pyroxenite in the origin
411 of the “garnet signature” in MORB. *Contributions to Mineralogy and Petrology*, 124, 185–
412 208.
- 413 Hofmeister, A.M., Fagan, T.J., Campbell, K.M., and Schaal, R.B. (1996) Single-crystal IR
414 spectroscopy of pyrope-almandine garnets with minor amounts of Mn and Ca. *American*
415 *Mineralogist*, 81, 418–428.
- 416 Hunt, S.A., Dobson, D.P., Li, L., Weidner, D.J., and Brodholt, J.P. (2010) Relative strength of
417 the pyrope-majorite solid solution and the flow-law of majorite containing garnets. *Physics*
418 *of the Earth and Planetary Interiors*, 179, 87–95.
- 419 Immoor, J., Marquardt, H., Miyagi, L., Lin, F., Speziale, S., Merkel, S., Buchen, J., Kurnosov,
420 A., and Liermann, H.P. (2018) Evidence for {100}<011> slip in ferropericlase in Earth’s
421 lower mantle from high-pressure/high-temperature experiments. *Earth and Planetary*
422 *Science Letters*, 489, 251–257.
- 423 Jiang, F., Speziale, S., Shieh, S.R., and Duffy, T.S. (2004) Single-crystal elasticity of andradite
424 garnet to 11 GPa. *Journal of Physics: Condensed Matter*, 16, S1041–S1052.
- 425 Karato, S., Wang, Z., and Fujino, K. (1994) High-temperature creep of yttrium-aluminum garnet
426 single crystals. *Journal of Materials Science*, 29, 6458–6462.
- 427 Karato, S., Wang, Z., Liu, B., and Fujino, K. (1995) Plastic deformation of garnets: systematics
428 and implications for the rheology of the mantle transition zone. *Earth and Planetary Science*
429 *Letters*, 130, 13–30.
- 430 Kavner, A. (2007) Garnet yield strength at high pressures and implications for upper mantle and
431 transition zone rheology. *Journal of Geophysical Research*, 112, 1–9.

- 432 Kavner, A., and Duffy, T.S. (2001) Strength and elasticity of ringwoodite at upper mantle
433 pressures. *Geophysical Research Letters*, 28, 2691–2694.
- 434 Kavner, A., Sinogeikin, S. V, Jeanloz, R., and Bass, J.D. (2000) Equation of state and strength of
435 natural majorite. *Journal of Geophysical Research: Solid Earth*, 105, 5963–5971.
- 436 Kunz, M., MacDowell, A.A., Caldwell, W.A., Cambie, D., Celestre, R.S., Domning, E.E.,
437 Duarte, R.M., Gleason, A.E., Glossinger, J.M., Kelez, N., and others (2005) A beamline for
438 high-pressure studies at the Advanced Light Source with a superconducting bending magnet
439 as the source. *Journal of Synchrotron Radiation*, 12, 650–658.
- 440 Lebensohn, R.A., and Tomé, C.N. (1994) A self-consistent viscoplastic model: prediction of
441 rolling textures of anisotropic polycrystals. *Materials Science and Engineering A*, 175, 71–
442 82.
- 443 Li, L., Long, H., Raterron, P., and Weidner, D. (2006) Plastic flow of pyrope at mantle pressure
444 and temperature. *American Mineralogist*, 91, 517–525.
- 445 Lin, F., Hilairet, N., Raterron, P., Addad, A., Immoor, J., Marquardt, H., Tomé, C.N., Miyagi, L.,
446 and Merkel, S. (2017) Elasto-viscoplastic self consistent modeling of the ambient
447 temperature plastic behavior of periclase deformed up to 5.4 GPa. *Journal of Applied*
448 *Physics*, 122.
- 449 Lundstrom, C.C., Gill, J., and Williams, Q. (2000) A geochemically consistent hypothesis for
450 MORB generation. *Chemical Geology*, 162, 105–126.
- 451 Lutterotti, L., Matthies, S., Wenk, H.-R., Schultz, A.S., and Richardson, J.W. (1997) Combined
452 texture and structure analysis of deformed limestone from time-of-flight neutron diffraction
453 spectra. *Journal of Applied Physics*, 81, 594–600.
- 454 Mainprice, D., Bascou, J., Cordier, P., and Tommasi, A. (2004) Crystal preferred orientations of

- 455 garnets: Comparison between numerical simulation and electron back-scattered diffraction
456 (EBSD) measurements in naturally deformed eclogites. *Journal of Structural Geology*, 26,
457 2089–2102.
- 458 Marquardt, H., and Miyagi, L. (2015) Slab stagnation in the shallow lower mantle linked to an
459 increase in mantle viscosity. *Nature Geoscience*, 8, 311–314.
- 460 McMillan, P., Akaogi, M., Ohtani, E., Williams, Q., Nieman, R., and Sato, R. (1989) Cation
461 disorder in garnets along the $\text{Mg}_3\text{Al}_2\text{Si}_3\text{O}_{12}$ - $\text{Mg}_4\text{Si}_4\text{O}_{12}$ join: An infrared, Raman and NMR
462 study. *Physics and Chemistry of Minerals*, 16, 428–435.
- 463 McNamara, A.K., Karato, S.-I., and van Keken, P.E. (2001) Localization of dislocation creep in
464 the lower mantle: Implications for the origin of seismic anisotropy. *Earth and Planetary
465 Science Letters*, 191, 85–99.
- 466 Merkel, S. (2002) Deformation of polycrystalline MgO at pressures of the lower mantle. *Journal
467 of Geophysical Research*, 107, 2271.
- 468 Merkel, S., and Yagi, T. (2005) X-ray transparent gasket for diamond anvil cell high pressure
469 experiments. *Review of Scientific Instruments*, 76, 046109.
- 470 Merkel, S., Wenk, H.-R., Badro, J., Montagnac, G., Gillet, P., Mao, H.K., and Hemley, R.J.
471 (2003) Deformation of $(\text{Mg}_{0.9}\text{Fe}_{0.1})\text{SiO}_3$ perovskite aggregates up to 32 GPa. *Earth and
472 Planetary Science Letters*, 209, 351–360.
- 473 Merkel, S., Kubo, A., Miyagi, L., Speziale, S., Duffy, T.S., Mao, H., and Wenk, H.-R. (2006)
474 Plastic deformation of MgGeO_3 post-perovskite at lower mantle pressures. *Science*, 311,
475 644–647.
- 476 Miyagi, L., Kunz, M., Knight, J., Nasiatka, J., Voltolini, M., and Wenk, H.R. (2008) In situ
477 phase transformation and deformation of iron at high pressure and temperature. *Journal of*

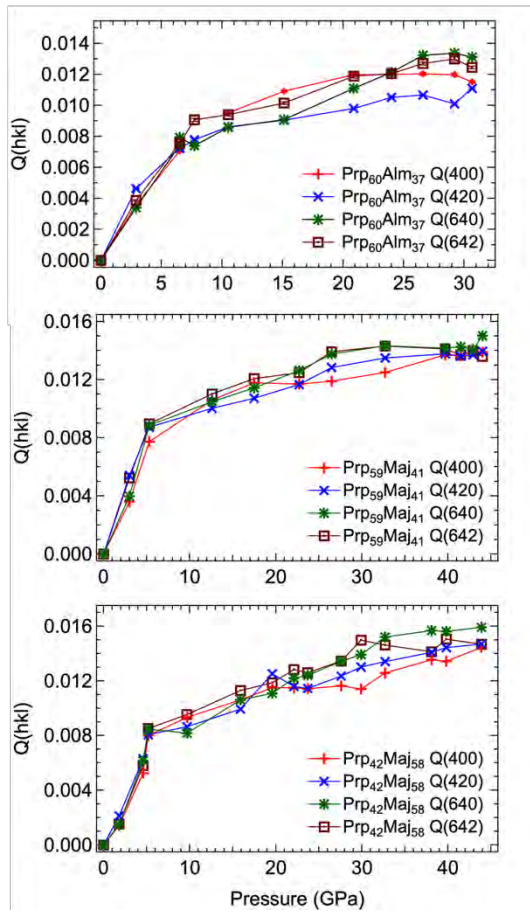
- 478 Applied Physics, 104.
- 479 Pacalo, R.E.G., and Weidner, D.J. (1997) Elasticity of majorite, MgSiO₃ tetragonal garnet.
480 Physics of the Earth and Planetary Interiors, 99, 145–154.
- 481 Popa, N.C., and Balzar, D. (2002) An analytical approximation for a size-broadened profile
482 given by the lognormal and gamma distributions. Journal of Applied Crystallography, 35,
483 338–346.
- 484 Prescher, C., and Prakapenka, V.B. (2015) *DIOPTAS*: a program for reduction of two-
485 dimensional X-ray diffraction data and data exploration. High Pressure Research, 1–8.
- 486 Ringwood, A.E. (1962) A model for the upper mantle. Journal of Geophysical Research, 67,
487 857–867.
- 488 Schmerr, N.C., Kelly, B.M., and Thorne, M.S. (2013) Broadband array observations of the 300
489 km seismic discontinuity. Geophysical Research Letters, 40, 841–846.
- 490 Singh, A.K., and Balasingh, C. (1993) The lattice strains in a specimen (cubic system)
491 compressed nonhydrostatically in an opposed anvil high pressure setup. Journal of Applied
492 Physics, 73, 4278–4286.
- 493 Singh, A.K., and Balasingh, C. (1994) The lattice strains in a specimen (hexagonal system)
494 compressed nonhydrostatically in an opposed anvil high pressure setup. Journal of Applied
495 Physics, 75, 4956–4962.
- 496 Singh, A.K., Balasingh, C., Mao, H., Hemley, R.J., and Shu, J. (1998) Analysis of lattice strain
497 measured under nonhydrostatic pressure. Journal of Applied Physics, 83, 7567–7575.
- 498 Sinogeikin, S. V., and Bass, J.D. (2000) Single-crystal elasticity of pyrope and MgO to 20 GPa
499 by Brillouin scattering in the diamond cell. Physics of the Earth and Planetary Interiors,
500 120, 43–62.

- 501 Sinogeikin, S. V, and Bass, J.D. (2002) Elasticity of majorite and a majorite-pyrope solid
502 solution to high pressure: Implications for the transition zone. *Geophysical Research*
503 *Letters*, 29, 1017.
- 504 Tian, Y., and Zhao, D. (2012) Seismic anisotropy and heterogeneity in the Alaska subduction
505 zone. *Geophysical Journal International*, 190, 629–649.
- 506 Turner, P.A., and Tomé, C.N. (1994) A study of residual stresses in Zircaloy-2 with rod texture.
507 *Acta Metallurgica et Metallica*, 42, 4143–4153.
- 508 Voegelé, V., Cordier, P., Sautter, V., Sharp, T.G., Lardeaux, J.M., and Marques, F.O. (1998a)
509 Plastic deformation of silicate garnets. II. Deformation microstructures in natural samples.
510 *Physics of the Earth and Planetary Interiors*, 108, 319–338.
- 511 Voegelé, V., Ando, J.I., Cordier, P., and Liebermann, R.C. (1998b) Plastic deformation of
512 silicate garnets I. High-pressure experiments. *Physics of the Earth and Planetary Interiors*,
513 108, 305–318.
- 514 Wang, H., Wu, P.D., Tomé, C.N., and Huang, Y. (2010) A finite strain elastic-viscoplastic self-
515 consistent model for polycrystalline materials. *Journal of the Mechanics and Physics of*
516 *Solids*, 58, 594–612.
- 517 Wenk, H.-R., Matthies, S., Donovan, J., and Chateigner, D. (1998) BEARTEX: A Windows-
518 based program system for quantitative texture analysis. *Journal of Applied Crystallography*,
519 31, 262–269.
- 520 Wenk, H.-R., Lutterotti, L., Kaercher, P., Kanitpanyacharoen, W., Miyagi, L., and Vasin, R.
521 (2014) Rietveld texture analysis from synchrotron diffraction images. II. Complex
522 multiphase materials and diamond anvil cell experiments. *Powder Diffraction*, 29, 220–232.
- 523 Williams, Q., and Revenaugh, J. (2005) Ancient subduction, mantle eclogite, and the 300 km

- 524 seismic discontinuity. *Geology*, 33, 1–4.
- 525 Xu, W., Lithgow-Bertelloni, C., Stixrude, L., and Ritsema, J. (2008) The effect of bulk
526 composition and temperature on mantle seismic structure. *Earth and Planetary Science*
527 *Letters*, 275, 70–79.
- 528 Zhang, J., and Green, H.W. (2007) Experimental investigation of eclogite rheology and its
529 fabrics at high temperature and pressure. *Journal of Metamorphic Geology*, 25, 97–115.

530

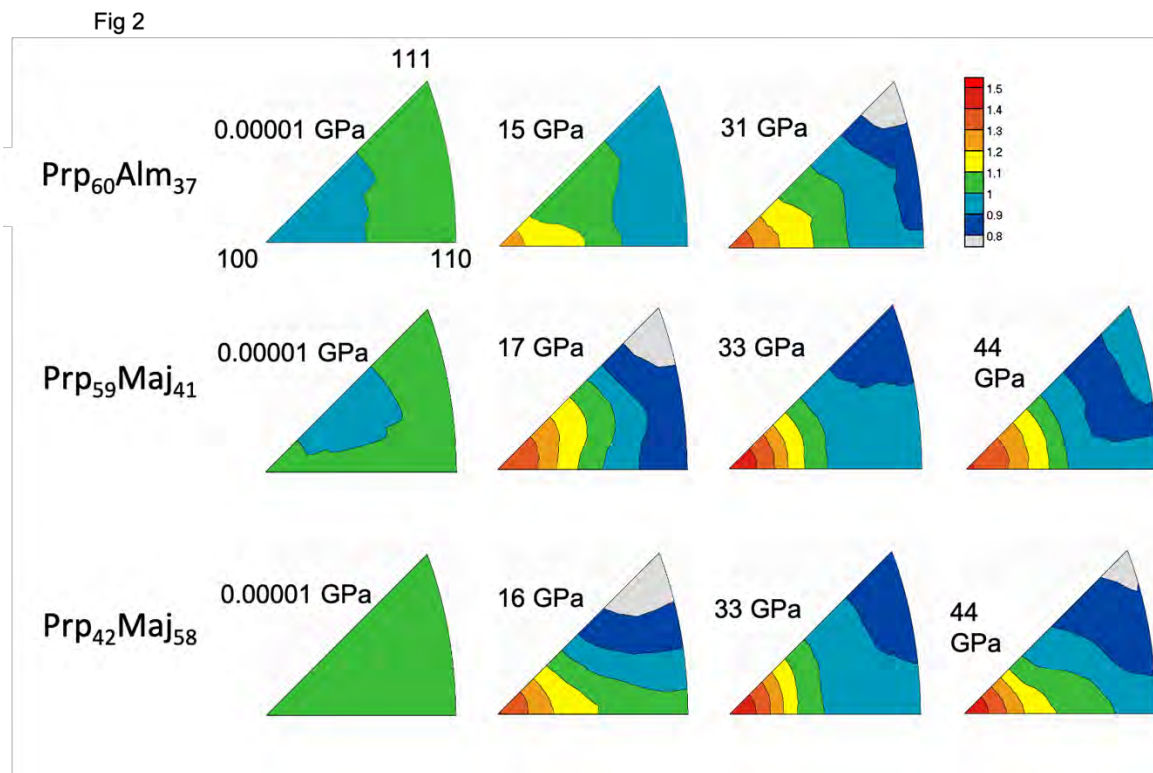
Fig 1



531

532 **Figure 1.** Experimental $Q(hkl)$ with increased pressure of the (400), (420), (640), and (642)

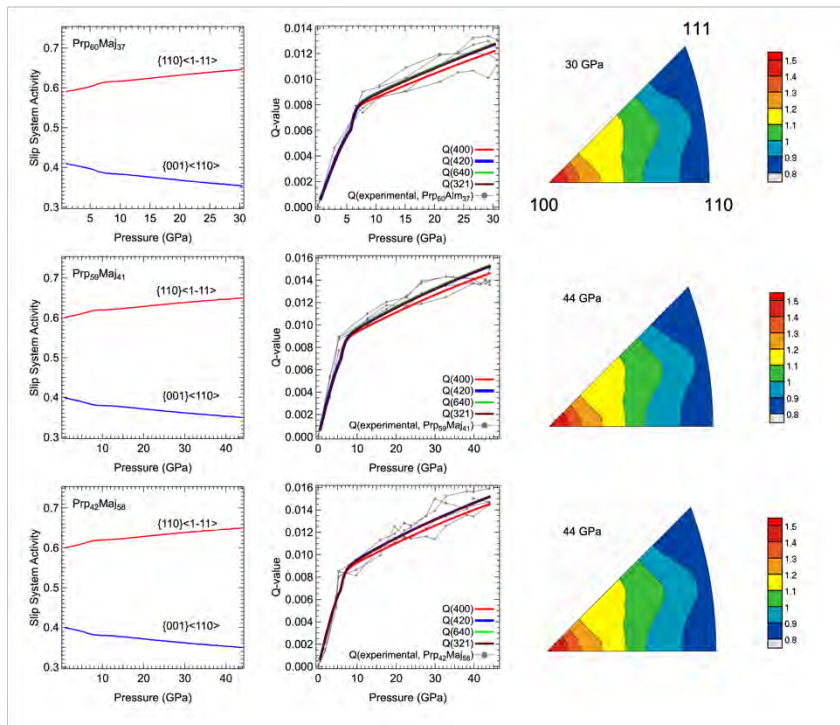
533 diffraction lines for (top) $\text{PrP}_{60}\text{Alm}_{37}$, (middle) $\text{PrP}_{59}\text{Maj}_{41}$, and (bottom) $\text{PrP}_{42}\text{Maj}_{58}$.



534

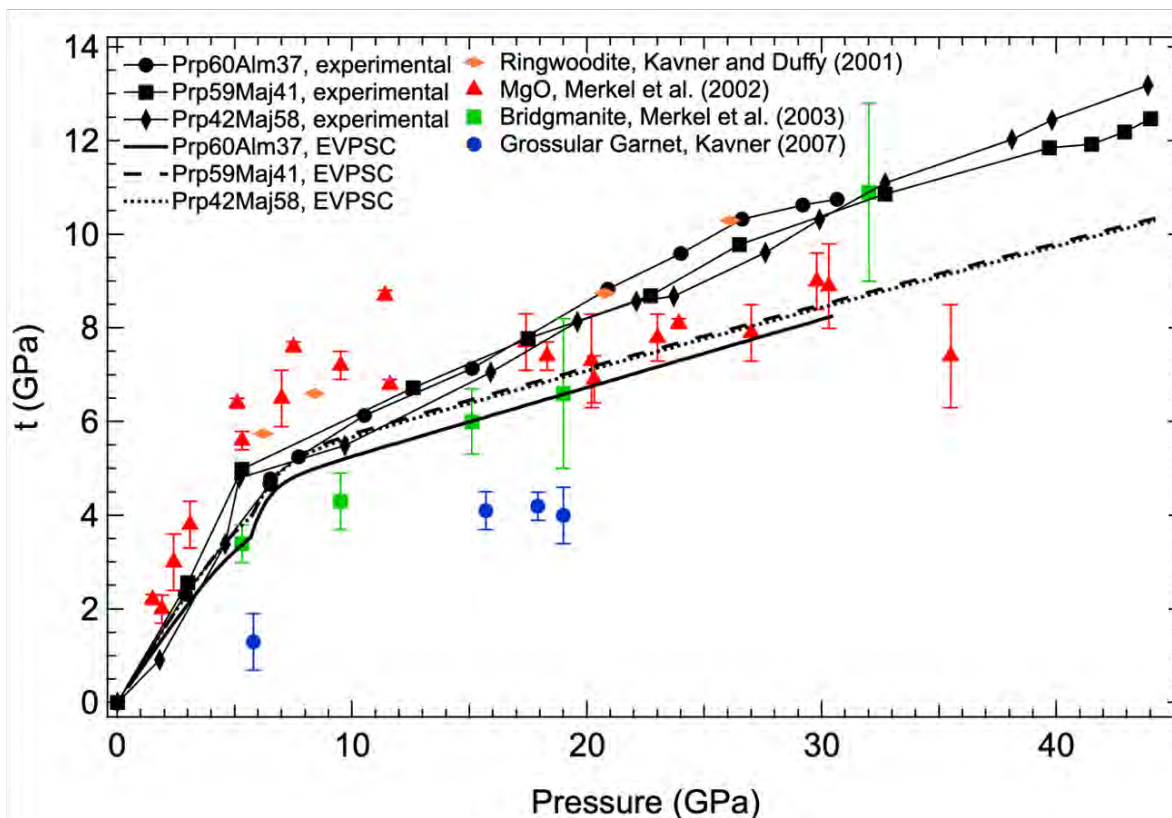
535 **Figure 2.** Representative inverse pole figures for the maximum compression direction of
536 Prp₆₀Alm₃₇, Prp₅₉Maj₄₁, and Prp₄₂Maj₅₈ at ambient pressure, ~16 GPa, ~31 GPa and 44 GPa.

Fig 3



537
 538 **Figure 3.** (left) Relative activity of slip systems with pressure; (middle) resulting Q -factors from
 539 active slip systems with pressure compared to experimental Q -factors; and (right) inverse pole
 540 figures for the maximum compression direction at the highest pressures probed for (top)
 541 Prp₆₀Alm₃₇, (middle) Prp₅₉Mj₄₁, (bottom) Prp₄₂Maj₅₈.
 542

Fig 4



543
544 **Figure 4.** A comparison between the strength as calculated with $t = 6G \langle Q(hkl) \rangle$, EVPSC
545 modeling, and other relevant mantle phases: bridgmanite (Merkel et al. 2003), MgO (Merkel
546 2002), grossular garnet (Kavner 2007), and ringwoodite (Kavner and Duffy 2001). Error bars for
547 this study are smaller than the symbols.
548